

A Machine Learning Approach to Classify Vortex Wakes of Energy Harvesting Oscillating Foils

Bernardo Luiz R. Ribeiro* and Jennifer A. Franck†
University of Wisconsin—Madison, Madison, WI, 53706

5 **A machine learning model is developed to establish wake patterns behind oscillating foils whose kinematics are within the energy harvesting regime. The role of wake structure is particularly important for array deployments of oscillating foils, since the unsteady wake highly influences performance of downstream foils. This work explores 46 oscillating foil kinematics, with the goal of parameterizing the wake based on the input kinematic variables and grouping vortex wakes through image analysis of vorticity fields. A combination of a convolutional neural**

10 **network (CNN) with long short-term memory (LSTM) units is developed to classify the wakes into three classes. To fully verify the physical wake differences among foil kinematics, a convolutional autoencoder combined with k-means++ clustering is utilized and four different wake patterns are found. With the classification model, these patterns are associated with a range of foil kinematics. Future work can use these correlations to predict the performance of foils placed in the wake and build optimal foil arrangements for tidal energy harvesting.** 

15

I. Introduction

This paper utilizes a machine learning approach to classify vortex wake structures behind an energy harvesting oscillating foil. Understanding the vortex formation and resulting wake structure reveals information about the upstream disturbance, which could potentially be linked to the underlying flow conditions and/or oscillating foil kinematics. Although commonly used in propulsive applications, oscillating foils can also extract energy from the flow in a 20 similar manner as a rotational turbine [1][2]. Furthermore, due to the coherent vortex wake of opposite vortex signs generated from the upstroke and downstroke foil motion there is a potential for cooperative motion within tightly packed array configurations to improve performance [3]. In order to create control laws to optimize performance in array configurations, it is critical to fully understand and model the wake structure as a function of flow conditions and foil kinematics.

25 Traditional wake structure characterization is commonly investigated for cylindrical bluff bodies, such as the canonical work of Williamson and Roshko [4] who described vortex wakes with a ' $mS + nP$ ' notation, where m is the number of single vortices (S) shed per cycle, and n is the number of clockwise/counter-clockwise vortex pairs (P). This notation has been propagated to oscillating foils with some success when the foil is in pure pitching [5][6] or plunging

*Graduate Research Assistant, Department of Engineering Physics, AIAA Student Member.

†Assistant Professor, Department of Engineering Physics, AIAA Senior Member.

‡Presented at the 2021 AIAA Aviation Forum, paper 2021-2947

[7] motion. However, previous investigations focused on kinematics for propulsive foils and did not consider the wakes generated by an oscillating foil in the energy harvesting regime. When used for energy harvesting, the foil kinematics are characterized by a lower non-dimensional frequency and higher pitch/heave amplitudes compared to oscillating foil propulsion. The high amplitudes result in a rich variety of wakes with multiple vortices shed each foil stroke that are often chaotic and not easily identified by the ‘ $mS + nP$ ’ notation [8, 9].

To assist in the wake modeling of bluff bodies outside the canonical characterization, various machine learning techniques can be utilized. Particularly, convolutional neural networks (CNN) receive much interest due to the ability to process data from images for pattern recognition and prediction [10]. For instance, a CNN is implemented to analyze cylinder and airfoil flow for various Reynolds numbers and obtained accurate predictions of the velocity field [11, 12] and force [13] when compared to numerical data. Another example of a CNN is for vortex identification procedure [14] which does not require user-input for thresholding such as Q -criterion [15] or λ_2 criterion [16].

When analyzing unsteady flows, the time evolution of structures can be captured with recurrent neural networks with the use of long short-term memory (LSTM) [17], which can predict flow quantities by holding information from an input sequence, and not simply from a single input [18]. Using flow information from the past five timesteps, Nakamura et al. [19] predicted turbulent structures in a channel flow using a convolutional autoencoder combined with LSTM. LSTM was also implemented in a dynamic wind farm wake model that predicts the main features of unsteady wind turbine wakes almost as well as high-fidelity computational models [20]. The integration of convolutional layers and LSTM units has also predicted unsteady flow fields behind bluff bodies such as a cylinder and a foil [18].

The goal of this investigation is to develop a neural network that integrates convolutional layers and LSTM units towards classification of the bluff body wake structures behind oscillating foils. Using such classification will enable predictive models for these chaotic wakes, and inform performance optimization of arrays of foils operating as energy harvesters. Classification models have been previously implemented for wakes of propulsive foils [21, 22] and cylinders [23]. This work classifies and clusters the drag-based wake from an oscillating foil in energy harvesting mode, which distinguishes itself from propulsive oscillating foils due to the lower oscillating frequency, higher pitch, and higher heave amplitudes [24]. Prior work has also largely classified wake structures from point measurements within the wake. In contrast, this research classifies vortex wake structures from vorticity flow fields. Using images as the input data allows for connections linking wake features such as the size and strength of vortices with the underlying foil kinematics. Due to the unsteady interactions between vortices that affect the wake trajectory behind each foil configuration, the LSTM network aims to provide information on how each wake image is linked throughout time, improving the classification outcomes. The results of the supervised classification groupings are compared directly against an unsupervised convolutional autoencoder (CAE) and clustering methodology [25] to confirm and update the boundaries between classes. Finally, the physics of the wake structure in each of the classified groups are explained and correlated with energy harvesting efficiency and foil kinematics.

Section [II](#) gives an overview of the foil kinematics and simulation methods followed by the initial groupings for the classification model in Section [III](#). An overview of the classification network architecture and results are presented in Section [IV](#), and Section [V](#) describes the groupings, and updates obtained from an unsupervised clustering of the input images with conclusions presented in Section [VI](#).

II. Computational Methods

This section discusses the computational fluid dynamics methods, including the foil kinematics, flow solver and mesh.

A. Foil Parameters

The foil kinematics are defined by three parameters, namely pitch amplitude, θ_o , heave amplitude, h_o , and reduced frequency, fc/U_∞ , where c is the foil's chord length and U_∞ , the freestream velocity. To generate a range of energy harvesting vortex wake structures, 46 unique kinematics are prescribed to a 10% thick elliptical foil through numerical simulations. The foil motion is sinusoidal in pitch and heave, utilizing a range of frequencies and amplitudes previously established as effective at energy harvesting [\[8, 26\]](#). As opposed to an airfoil geometry, a thin elliptical foil is utilized as geometry has shown to have minor effects on efficiency [\[27\]](#) and the fore-aft symmetry is desirable for harvesting energy from tidal flows. The kinematics with respect to time t are described in lab-fixed coordinates as

$$h(t) = -h_o \cos(2\pi ft) \quad (1)$$

and

$$\theta(t) = -\theta_o \cos(2\pi ft + \pi/2), \quad (2)$$

where $h(t)$ and $\theta(t)$ are the prescribed heave and pitch motions, respectively, with pitching about the center-chord. The phase difference between pitch and heave is fixed at $\pi/2$, which is found to yield the optimal energy harvesting performance [\[28\]](#). At $t = 0$ the foil is at the bottom of its heave stroke. Heave and pitch are changing simultaneously during foil motion, which creates a time-varying relative angle of attack with respect to the freestream flow given by

$$\alpha_{rel}(t) = \tan^{-1}(-\dot{h}(t)/U_\infty) + \theta(t), \quad (3)$$

with $\dot{h}(t)$ representing the time derivative of the heave motion. A characteristic relative angle of attack is evaluated when the foil is at maximum pitch and maximum heave velocity, which occurs at one quarter of the cycle period T , or

$$\alpha_{T/4} = \alpha_{rel}(t/T = 0.25) = \tan^{-1}(-2\pi f h_0/U_\infty) + \theta_0. \quad (4)$$

The foil motion along with the foil parameters are illustrated in Figure 1. The primary vortex, or the first vortex
85 formed on the suction surface during each half stroke, is highlighted for the case $fc/U_\infty = 0.10$; $h_o = 1.00$; $\theta_o = 75^\circ$.
Previous vortices originating from prior oscillating cycles provide an overall view of the wake.

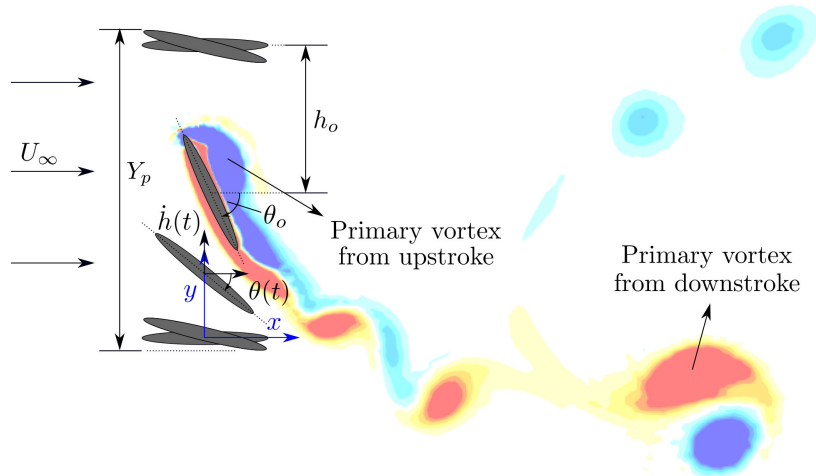


Fig. 1 Foil kinematics: pitch amplitude (θ_o), heave amplitude (h_o) and foil's swept area (Y_p) shown. Spanwise vorticity at non-dimensional time $t/T = 0.50$ for the kinematics $fc/U_\infty = 0.10$; $h_o = 1.00$; $\theta_o = 75^\circ$ is displayed as an example of the oscillating foil wake.

To evaluate performance the energy harvesting efficiency is defined as

$$\eta = \frac{\bar{P}}{\frac{1}{2}\rho U_\infty^3 Y_p}, \quad (5)$$

which is the ratio of the average power extracted, \bar{P} , to the power available in the freestream velocity throughout the swept area Y_p . The power extracted is defined as

$$P(t) = F_y \dot{h} + M_z \dot{\theta}, \quad (6)$$

90 where F_y and M_z are the vertical force and spanwise moment on the foil, respectively. To remove small cycle-to-cycle variations the efficiency is phase-averaged over the last three cycles of simulation.

A wide range of kinematics within the energy harvesting regime is considered, all of which directly influence $\alpha_{T/4}$. Table I outlines all simulated foil kinematics, with seven sets of different kinematics chosen specifically with the same $\alpha_{T/4}$. All quantities reported in this manuscript are non-dimensionalized by the freestream velocity, U_∞ , and

95 c and thus, $f^* = fc/U_\infty$ and $h_o^* = h_o/c$. Reduced frequency, pitch amplitude and heave amplitude are varied from $f^* = 0.10 - 0.15$, $\theta_o = 40^\circ - 80^\circ$, $h_o^* = 0.50 - 1.50$.

Kinematics	$\alpha_{T/4}$	Kinematics	$\alpha_{T/4}$
$(*,+)$ $f^* = 0.15; h_o^* = 1.25; \theta_o = 55^\circ$	5.3°	$f^* = 0.12; h_o^* = 0.50; \theta_o = 50^\circ$	29.3°
$(*,+)$ $f^* = 0.12; h_o^* = 1.50; \theta_o = 55^\circ$	6.5°	$f^* = 0.10; h_o^* = 0.75; \theta_o = 55^\circ$	29.8°
$(*,+)$ $f^* = 0.15; h_o^* = 1.00; \theta_o = 50^\circ$	6.7°	$(*,+)$ $f^* = 0.12; h_o^* = 0.75; \theta_o = 60^\circ$	30.5°
$(+)$ $f^* = 0.10; h_o^* = 1.00; \theta_o = 40^\circ$	7.9°	$(*,+)$ $f^* = 0.15; h_o^* = 1.00; \theta_o = 75^\circ$	31.7°
$(*,+)$ $f^* = 0.12; h_o^* = 1.00; \theta_o = 45^\circ$	8.0°	$(*,+)$ $f^* = 0.12; h_o^* = 1.25; \theta_o = 75^\circ$	31.7°
$f^* = 0.15; h_o^* = 0.75; \theta_o = 45^\circ$	9.8°	$f^* = 0.10; h_o^* = 0.50; \theta_o = 50^\circ$	32.6°
$(*,+)$ $f^* = 0.12; h_o^* = 0.75; \theta_o = 40^\circ$	10.5°	$(*,+)$ $f^* = 0.10; h_o^* = 1.00; \theta_o = 65^\circ$	32.9°
$(*,+)$ $f^* = 0.15; h_o^* = 1.00; \theta_o = 55^\circ$	11.7°	$f^* = 0.12; h_o^* = 0.50; \theta_o = 55^\circ$	34.3°
$(*,+)$ $f^* = 0.10; h_o^* = 1.00; \theta_o = 45^\circ$	12.9°	$f^* = 0.10; h_o^* = 0.75; \theta_o = 60^\circ$	34.8°
$(+)$ $f^* = 0.12; h_o^* = 1.00; \theta_o = 50^\circ$	13.0°	$(*,+)$ $f^* = 0.12; h_o^* = 0.75; \theta_o = 65^\circ$	35.5°
$(*,+)$ $f^* = 0.10; h_o^* = 0.75; \theta_o = 40^\circ$	14.8°	$f^* = 0.15; h_o^* = 1.00; \theta_o = 80^\circ$	36.7°
$(*,+)$ $f^* = 0.15; h_o^* = 1.00; \theta_o = 60^\circ$	16.7°	$f^* = 0.10; h_o^* = 0.50; \theta_o = 55^\circ$	37.6°
$(+)$ $f^* = 0.12; h_o^* = 1.00; \theta_o = 55^\circ$	18.0°	$(*,+)$ $f^* = 0.12; h_o^* = 1.00; \theta_o = 75^\circ$	38.0°
$f^* = 0.12; h_o^* = 0.50; \theta_o = 40^\circ$	19.3°	$f^* = 0.12; h_o^* = 0.50; \theta_o = 60^\circ$	39.3°
$(*,+)$ $f^* = 0.10; h_o^* = 0.75; \theta_o = 45^\circ$	19.8°	$f^* = 0.12; h_o^* = 0.75; \theta_o = 70^\circ$	40.5°
$(+)$ $f^* = 0.12; h_o^* = 0.75; \theta_o = 50^\circ$	20.5°	$f^* = 0.10; h_o^* = 1.25; \theta_o = 80^\circ$	41.9°
$(*,+)$ $f^* = 0.12; h_o^* = 1.25; \theta_o = 65^\circ$	21.7°	$(*,+)$ $f^* = 0.10; h_o^* = 1.00; \theta_o = 75^\circ$	42.9°
$(*,+)$ $f^* = 0.10; h_o^* = 1.25; \theta_o = 60^\circ$	21.9°	$f^* = 0.12; h_o^* = 1.00; \theta_o = 80^\circ$	43.0°
$f^* = 0.12; h_o^* = 1.00; \theta_o = 60^\circ$	23.0°	$f^* = 0.10; h_o^* = 0.75; \theta_o = 70^\circ$	44.8°
$f^* = 0.12; h_o^* = 0.50; \theta_o = 45^\circ$	24.3°	$(*,+)$ $f^* = 0.10; h_o^* = 0.50; \theta_o = 65^\circ$	47.6°
$(*,+)$ $f^* = 0.15; h_o^* = 1.25; \theta_o = 75^\circ$	25.3°	$f^* = 0.10; h_o^* = 1.00; \theta_o = 80^\circ$	47.9°
$(*,+)$ $f^* = 0.15; h_o^* = 1.00; \theta_o = 70^\circ$	26.7°	$f^* = 0.12; h_o^* = 0.50; \theta_o = 70^\circ$	49.3°
$(+)$ $f^* = 0.12; h_o^* = 1.00; \theta_o = 65^\circ$	28.0°	$f^* = 0.12; h_o^* = 0.75; \theta_o = 80^\circ$	50.5°

+ Training data, $*,+$ First cycle in validation data and remaining two cycles are used in the training data

Table 1 Summary of all kinematics with their computed $\alpha_{T/4}$ values. Footnote refers to the unsupervised clustering model.

B. Flow Solver and Mesh

The computations utilize an incompressible Navier-Stokes solver performed using a second-order accurate finite volume, pressure-implicit split-operator (PISO) method implemented in *OpenFOAM* [29]. The Reynolds number of $Re_c = 1000$ is selected for all simulations to enable a broad sweep of 46 kinematics within a tractable computational time. Prior work comparing experiments with low and high Reynolds number simulations has demonstrated only minor differences between the power generation and wake characteristics across a Reynolds number regime of $1000 - 50,000$ [8, 9].

All simulations are performed with a 2D unstructured mesh, with foil motion generated through the boundary condition of a dynamic mesh solver that updates the position of all nodes in the domain at every timestep. The dynamic mesh algorithm utilized in this manuscript is previously validated against a stationary mesh in the work from Ribeiro et al. [9]. The total domain size is $106c$ in the horizontal direction and $100c$ in the vertical direction, with the foil located $50c$ upstream in the x direction and vertically centered when the foil is at the bottom of its heave stroke ($t/T = 0$). The mesh is generated using Gmsh [30], with a subset of the mesh displayed in Figure 2.

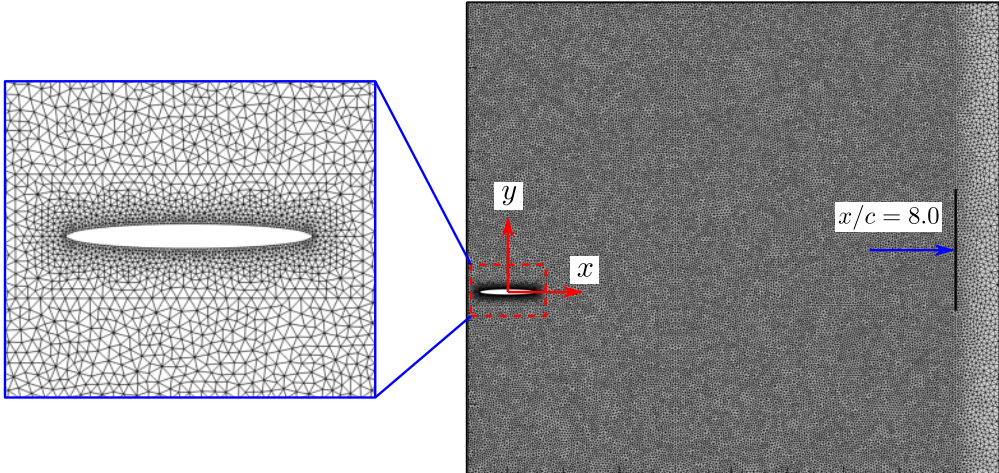


Fig. 2 Computational domain zoomed in on the foil mesh. The mesh 3A is displayed with its characteristics outlined in Table 2.

The boundary conditions entail a no-slip condition at the foil surface with zero pressure gradient, inlet flow on the left boundary, and outlet flow on the top, bottom and right boundaries. Simulations are run for a total of six oscillation cycles, and become stationary after three cycles.

Mesh refinement is evaluated through eight meshes with varying resolution near-foil and in the wake, where N corresponds to the total number of nodes. All mesh characteristics are displayed in Table 2 where the characteristic wake resolution is measured at $x/c = 3.0$; $y/c = 0$. This resolution is held approximately constant until $8c$ downstream as displayed in Figure 2. Along the foil surface, a characteristic Δx is measured along the mid-chord, and N_θ represents the total number of nodes on the body in the azimuthal direction. The CPU time is calculated for one oscillation cycle

using a single processor on the Intel Cascade architecture.

Table 2 Mesh characteristics.

Mesh	Wake		Foil		η	CPU time (hrs)
	N	Δx	N_θ	Δx		
Mesh 1A	0.30×10^5	0.14	150	0.013	29.3%	1.6
Mesh 2A	0.48×10^5	0.10	150	0.013	29.7%	1.8
Mesh 3A	1.64×10^5	0.05	150	0.013	26.9%	12.8
Mesh 4A	3.66×10^5	0.03	150	0.013	25.7%	41.2
Mesh 1B	0.31×10^5	0.14	240	0.008	30.7%	1.5
Mesh 2B	0.49×10^5	0.10	240	0.008	29.9%	2.1
Mesh 3B	1.56×10^5	0.05	240	0.008	26.9%	11.3
Mesh 4B	3.68×10^5	0.03	240	0.008	25.4%	40.0

Foil efficiency and spanwise vorticity flow fields are evaluated across all meshes. Foil efficiency decreases with increasing wake resolution, demonstrating a $\Delta\eta$ of 3% between mesh 2 and mesh 3 which has twice the wake resolution. As shown in the vorticity fields, the same number of coherent vortices are observed between meshes 3 and 4, with only small variations in vortex positioning in the wake as displayed in Figure 3. There is little difference between meshes A and B, indicating both have sufficient near-foil resolution. Therefore, as a balance in computational cost and accuracy of both the foil forces and flow fields, mesh 3A is utilized in all simulations.

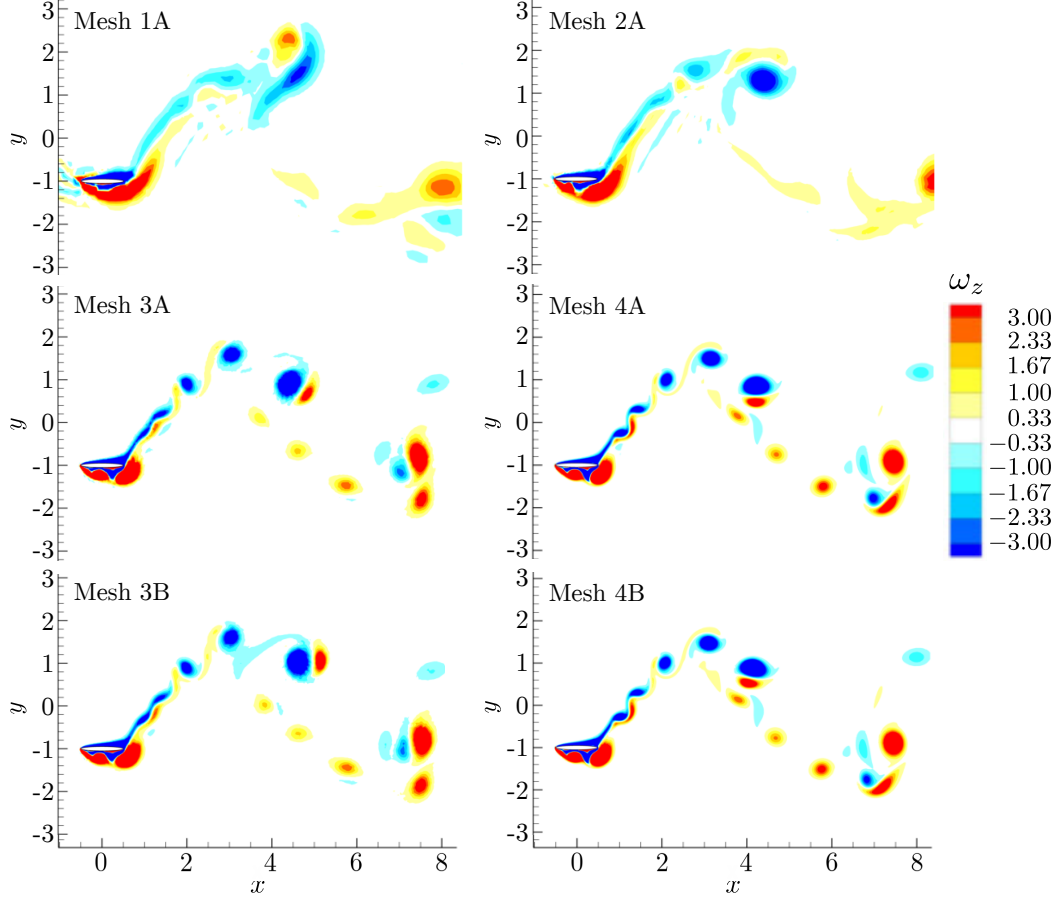


Fig. 3 Instantaneous vorticity field in the z direction, ω_z . Kinematics: $f^* = 0.12$; $h_o^* = 1.00$; $\theta_o = 65^\circ$.

125

III. Initial Class Selection

The kinematics outlined in Table I cover a large parameter space, which contributes to a range of energy harvesting modes, which range in efficiency from close to zero up to 30%. These results demonstrate that the optimal performance is not strongly correlated with a single set of foil kinematics. As displayed in Figure 4a high energy harvesting efficiency is found within the range $f^* = 0.12 - 0.15$; $\theta_o = 65^\circ - 80^\circ$; $h_o^* = 0.50 - 1.00$ with no clear correlation with a single 130 kinematic parameter. Thus, it is convenient to reduce the parameter space into a single and representative variable, $\alpha_{T/4}$, the characteristic relative angle of attack as defined in Equation 4, which allows foil efficiency to be expressed as a simpler function of foil kinematics as shown in Figure 4b [26]. The efficiency increases monotonically until $\alpha_{T/4} \approx 28.0^\circ$ and then varies for higher $\alpha_{T/4}$ values due to a high degree of flow separation [8, 9].

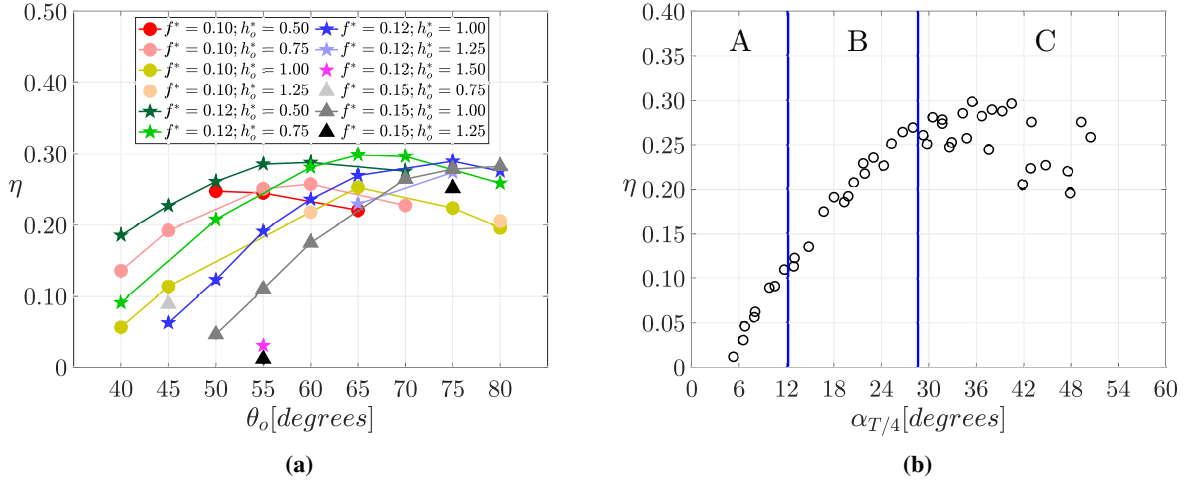


Fig. 4 (a) Energy harvesting efficiency, η , as a function of pitch amplitude, θ_o (in degrees) for various reduced frequency (f^*) and heave amplitude (h_o^*) pairs; (b) Efficiency with respect to $\alpha_{T/4}$. Vertical lines indicate initial grouping of vortex wake structures based on primary vortex strength analysis.

To correlate $\alpha_{T/4}$ with the flow structures that emanate from the foil, Ribeiro et al. [9] defined three classes labeled 135 A ($5.3^\circ \leq \alpha_{T/4} \leq 11.7^\circ$), B ($11.7^\circ < \alpha_{T/4} < 29.3^\circ$) and C ($29.3^\circ \leq \alpha_{T/4} \leq 50.5^\circ$) using the maximum strength of the primary vortex formed for each kinematics (as demonstrated in Figure 4b). The wake structures that emerge from the three classes are displayed in Figure 5 within a $7.5c$ by $7.5c$ window located downstream, and general trends based on vortex strength are extracted from these wakes. Class A contains weak vortices as represented by a shear layer in the majority of images in this class. In contrast, class C displays the strongest and most coherent vortices compared with the 140 other classes. Class B has a mix of kinematics with stronger vortices than class A but weaker than class C.

Observing the wake structures from Figure 5, trends are found within and between classes. With an increase in pitch amplitude, vortices shed from the foil increase in size and strength with frequency and heave amplitude $f^* = 0.12; h_o^* = 0.50$ (see kinematics highlighted in red). With an increase in reduced frequency, the wake wavelength is smaller as displayed by the kinematics with $h_o^* = 1.25, \theta_o = 75^\circ$ (see kinematics in green).

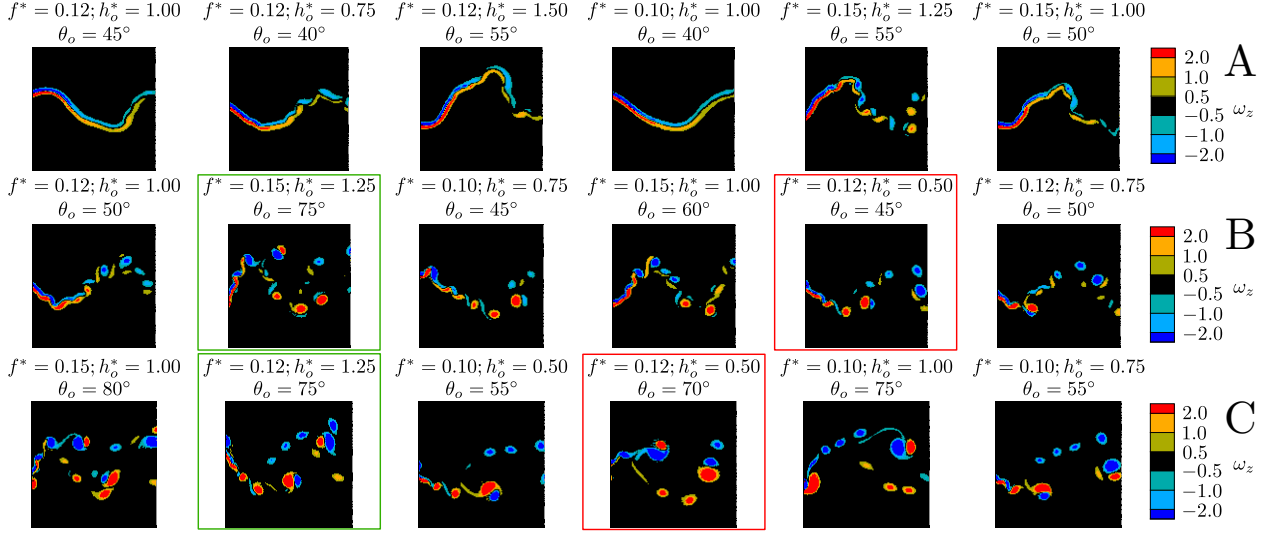


Fig. 5 Randomly selected images of wake structures from each class highlighted in Figure 4b. The colored boxes outline wake features found when one foil parameter is varied while others remain constant.

145

IV. Supervised Classification

In this Section, the wake is analyzed through an image-based supervised learning algorithm, where classes are defined based on the predetermined groupings motivated in Section III.

A. Data Pre-Processing

The input to the classification model are images of 2D spanwise vorticity extracted from a $7.5c$ by $7.5c$ window 150 located in the wake and interpolated onto a cartesian grid of 128 by 128 pixels as illustrated in Figure 6. The window size is selected such that it contains all vortices shed from the foil in the y -direction in all kinematics from Table I and $7.5c$ corresponds to a typical inter-foil spacing in foil-arrays under the energy harvesting regime. For each set of kinematics, three oscillation cycles within the steady state regime are used as input with data sampled at every $tU_\infty/c = 0.1$, for a total of 11,846 samples. The fixed sampling rate is used in order to maintain the difference between consecutive wake 155 images independent of the foil's reduced frequency, thus the number of samples differs for each frequency. Contour levels of vorticity are chosen to display the wake structures in all kinematics, and six levels ($-2, -1, -0.5, 0.5, 1, 2$) are consistently drawn for each wake image as shown in Figure 6.

Since the vortices shed from the foil may affect each other's trajectory [9, 31, 32], the time evolution is considered in the classification neural network through the use of LSTM units. A sequence of five images is given as the input data, 160 which provided higher accuracy compared with a sequence of ten images. To avoid overfitting, a data augmentation technique is also implemented, which duplicated the number of samples from 11,846 to 23,692. This technique not only took an input sequence at consecutive $0.1tU_\infty/c$ units, but also with $0.1tU_\infty/c$ skipped between samples, i.e. 0.1, 0.3, 0.5, 0.7, 0.9 tU_∞/c , following a similar strategy by Chong and Tay [33].

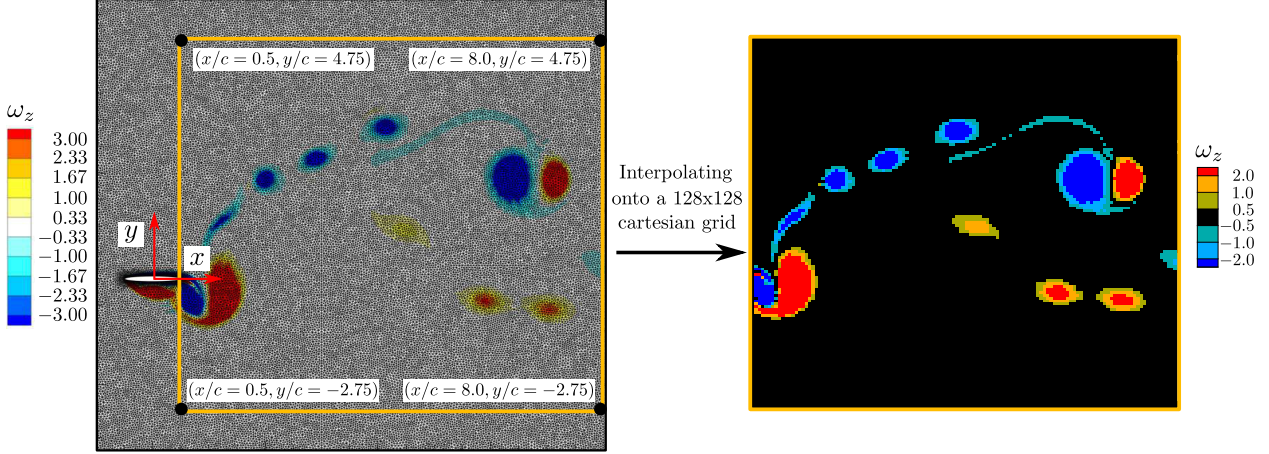


Fig. 6 Data pre-processing for the classification model interpolates the spanwise vorticity computed with high resolution computational data onto a 128x128 grid for a fixed region behind the foil at every 0.1 convective time units.

B. Classification Model Architecture

Using the Python based libraries TensorFlow [34] and Keras [35], the classification model is built from a combination of convolutional layers, LSTM units and dense layers, as outlined in Figure 7. The 2D convolutional layers (*Conv2D*) are applied on each sample to extract the most significant features of the wake. These key features are detected with filters, which create feature maps through a convolutional operation on the preceding layer [25]. Each convolutional layer uses a linear activation function with multiple filters of fixed kernel size, 3×3 , that reduces the matrix dimensions while simultaneously keeping the most pertinent features. The number of feature maps define the depth of each convolutional layer and within each layer, a downsample operation is performed with a 2×2 stride, resulting in a reduction factor of 2 in each matrix dimension while the depth remains constant. Each input sequence passes through four convolutional layers, decreasing the dimension of each sample from $128 \times 128 \times 1$ to an 8×8 feature map with eight channels.

Each sample is then flattened into a 1D vector with 512 elements where 90 LSTM units analyze the correlation between each wake image within the input sequence, with the goal of detecting patterns between each wake structure and its time evolution behind each foil configuration. The final section of the model contains a dropout layer of rate equals to 0.1 that is placed between two dense layers in order to decrease overfitting. The dense layers classify each image according to the predetermined classes. The first layer contains 90 neurons and the second dense layer has three neurons corresponding to class A, B or C. Both dense layers use a sigmoid activation function to normalize the output from the previous layer into a $0 - 1$ range. To update the neural network weights, the Adam optimization algorithm [36] is implemented in the model. To prevent overfitting, the early stopping technique [37] with 100 training epochs is utilized.

The following hyperparameters in the classification model are tuned: number of filters in the convolutional layers, LSTM units, and number of neurons in the first dense layer. The sequences of $(64, 32, 16, 8)$, $(32, 16, 8, 4)$,

(128, 64, 32, 16) filters for the convolutional layers are tested and (64, 32, 16, 8) obtained best performance. The LSTM
185 units and number of neurons in the first dense layer are tuned using a range from 20 – 100 units and neurons and it is found that 90 units and 90 neurons provided a higher model accuracy.

C. Model Accuracy in Predicting Class Label of Test Data

A five-fold stratified cross-validation is performed in the data, comprised of matrices of the vorticity fields and their respective class labels. This procedure helps decrease overfitting and it assures representative information of all
190 prelabeled classes in each test subset [35, 38, 39].

Using the three classes defined in Section III (see Figure 4b), the model is trained and an average accuracy of 92% is obtained across the five folds. This indicates that approximately 92% of all samples processed by the algorithm are labelled the same as their prelabels.

A confusion matrix, which is a common tool for summarizing the performance of a classification algorithm, and
195 the corresponding mislabeled test data distribution for the worst performance fold (fold 4) are shown in Figure 8. The algorithm does well discerning the kinematics within the class C but higher discrepancies are found for the classes A and B, with 11% mislabeled samples in class A and 37% in class B (29% + 8%). While the stratified cross-validation ensures a commensurate number of samples of each class in the training and test subsets, it does not ensure that each
200 individual kinematics is represented in every test subset. The test data distribution in Figure 8b highlights the kinematics that have a label mismatch. The orange bar corresponds to the 29% mislabeled samples that are classified as class A rather than class B, whereas red and pink bars show those mislabeled in classes B and C, respectively. Even though the mismatch percentages are high, there is only a single kinematics in fold 4 ($\alpha_{T/4} = 13.0^\circ$) that contains more than 50% label mismatch, and the corresponding $\alpha_{T/4}$ is close to the class boundary between classes A and B ($\alpha_{T/4} = 11.7^\circ$), which can explain the high mismatch.

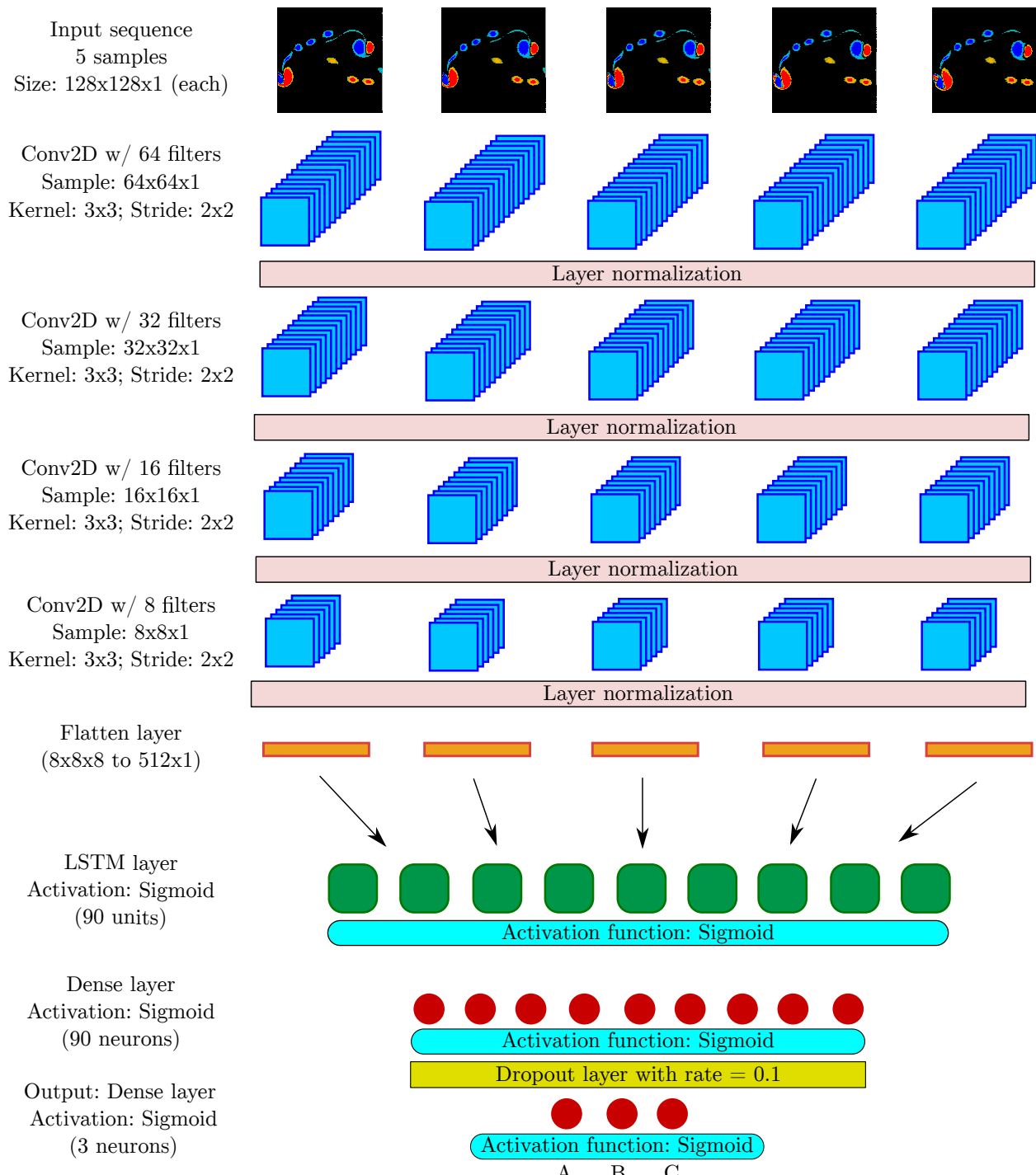


Fig. 7 Classification model architecture.

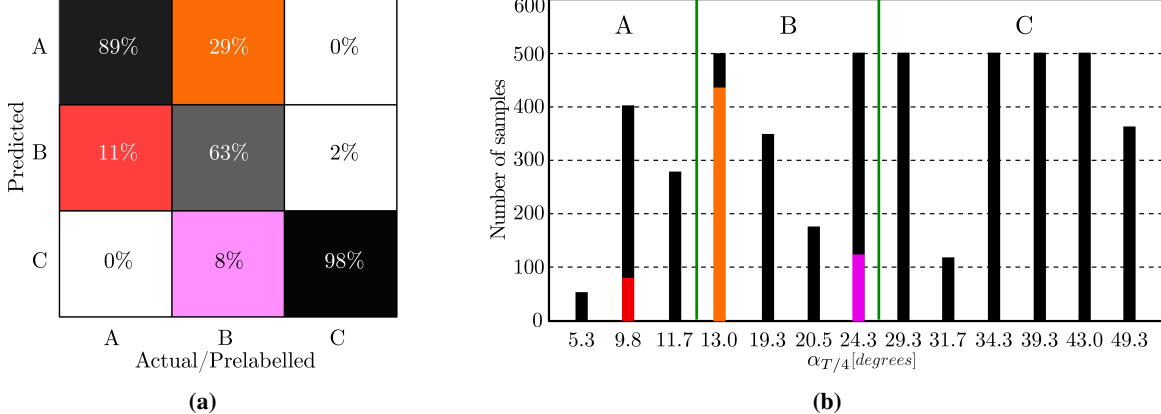


Fig. 8 (a) Confusion matrix for the worst performance (fold 4) with mislabeled class A samples colored in red; mislabeled class B in orange and in pink. (b) Test set distribution of all foil kinematics in number of samples among $\alpha_{T/4}$ values presented in fold 4. Only a single foil kinematics had more than 50% of images with a label mismatch between actual and predicted. The green lines divide the foil kinematics presented in each class.

205

V. Unsupervised Clustering

The classification model presented in Section IV divides the wake kinematics into three classes predetermined by the researcher (based on prior vortex analysis). In this Section, an unsupervised algorithm is utilized to group similar wake kinematics, and the clusters are subsequently compared with the classes from the supervised model. The unsupervised clustering groups the vortex images, individually, without any prior knowledge or relationship between wake kinematics 210 and the respective wake structures. Therefore, the clusters obtained through this method will assist in verifying the classification results and potentially modifying the class boundaries determined by the researcher.

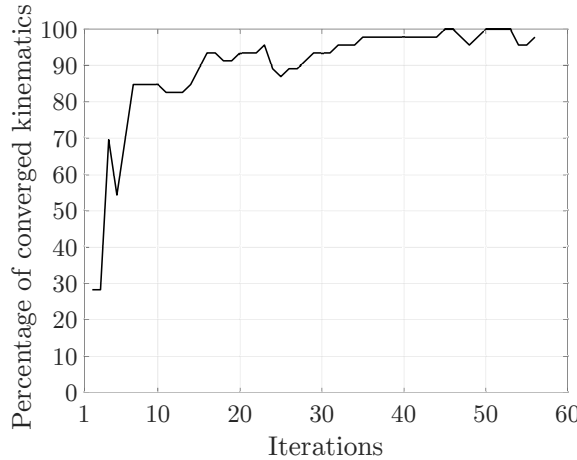
A. Clustering Model Architecture and Convergence

The unsupervised model architecture follows closely from the CAE clustering algorithm by Calvet et al. [25], including the same number of convolutional layers, filter and skip connections. The architecture consists of an 215 autoencoder with five sequences of convolutional and max-pooling layers for the encoder portion. For the decoder portion, five sequences of convolutional and up sampling layers are used. The only hyperparameter retuned is the batch size, in which an online learning method (batch size equals to 1), is implemented within the autoencoder. With this algorithm there is no prelabeling of images, but the user must determine the number of clusters, which is explained below.

220 The input data is the same vorticity images described in Section IV except that there are no time sequences provided, and therefore each instantaneous wake image is treated independently. This results in 11,846 unique samples from 46 simulations. The training and validation data for the autoencoder utilize 27 of the 46 simulated kinematics. Within the 27 kinematics, approximately 30% of the samples are used for validation, corresponding to the first out of the three oscillation cycles, as outlined in Table I. Using samples of the same foil kinematics in the training/validation sets

225 improved performance of the autoencoder while retuning. The remaining sets of foil kinematics (19) are used as test data after the autoencoder is tuned.

230 Due to the stochastic nature of the model, the CAE clustering algorithm is trained for multiple iterations to check for convergence under a developed criteria. After each independent iteration, a set of kinematics is designated to the cluster that contains the majority of its samples (since samples are treated independently, samples from the same kinematics can end up in different clusters). For each iteration, the cluster label at which a set of kinematics is assigned to is recorded. Convergence is reached if a set of kinematics remains in the same cluster (same label) as the previous iteration. Figure 9 shows the percentage of foil kinematics that converged when four clusters are considered. A total of 56 random clusterings is performed and after 35 iterations, the algorithm consistently maintains convergence of at least 96% of all foil kinematics being assigned to a unique cluster.



235 **Fig. 9 Convergence of the autoencoder and clustering model.**

240 A combination of the elbow and the silhouette score methods are utilized to determine the optimal number clusters for the provided samples, following the approach from Calvet et al. [25]. The elbow method [40] computes the total within-cluster sum of square error, known as distortion, and the number closer to the ‘elbow’ of the curve is the indicator of the approximate number of clusters that best separates the data. The silhouette score method [41] determines how well each image lies within its cluster by estimating cohesion (intra-class) and separation (inter-class) as Euclidean distances. The score is a combination of both factors, and ranges from zero to one, where a higher score indicates better clustering. The distortion and silhouette scores are averaged over all iterations with results displayed in Figure 10. The elbow, represented by the intersection point of the tangent dashed lines to both ends of the distortion curve in Fig. 10, is located between four and five clusters (see green shaded region) but a slightly higher silhouette score is found when the data is divided into four clusters. Therefore, the optimal number of clusters is set to four. Due to the small differences 245 in the averaged silhouette score, an analysis is also performed using five clusters but does not provide any additional

physical insights on wake patterns compared with four clusters.

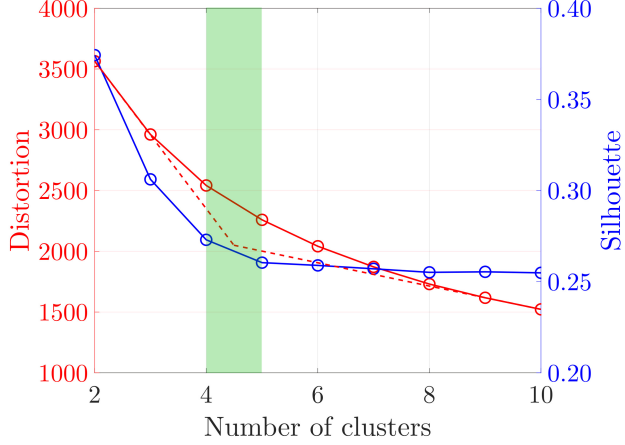


Fig. 10 Distortion (red solid line) and silhouette score (blue solid line) with respect to number of clusters and averaged over all iterations. The red dashed lines are tangent to both ends of the distortion line and their intersection point corresponds to the distortion curve's elbow. The green shaded region displays the numbers of clusters that are closest to the elbow.

B. Updating Class Boundaries Using the Clustering Results

The results of four clusters are displayed in Figure 11a. Every cluster is roughly defined within an $\alpha_{T/4}$ range, which is consistent with the results from the supervised model that also utilized $\alpha_{T/4}$ as the preferential kinematic parameter.

250 The clustering division of four clusters, rather than three, naturally imposes a new boundary and introduces small shifts in the other two cluster boundaries. These new divisions are explored by utilizing the previously described classification algorithm in the following manner.

For instance, the cluster A groups foil kinematics in the range of $\alpha_{T/4} \leq 14.8^\circ$ (Figure 11a), whereas the previous class A included kinematics with $\alpha_{T/4} \leq 11.7^\circ$. The proposed clustering division is implemented within the classification algorithm previously described (with the five-fold cross-validation). The results were less accurate, indicating that the classification algorithm can more reliably group images when the boundary is closer to $\alpha_{T/4} \leq 11.7^\circ$.

260 Similar tests are performed on the remaining two cluster-informed divisions at $\alpha_{T/4} = 24.3^\circ$ and $\alpha_{T/4} = 31.7^\circ$. The results indicate that shifting both these boundaries to slightly lower $\alpha_{T/4}$ reveals more accurate classification of images. These results inform the update on the class boundaries as proposed by the orange solid lines in Figure 11b, which are contrasted with the original classifications from Section IV (dashed blue lines). The orange shaded regions next to each boundary represent the mismatch between the class and cluster boundaries.

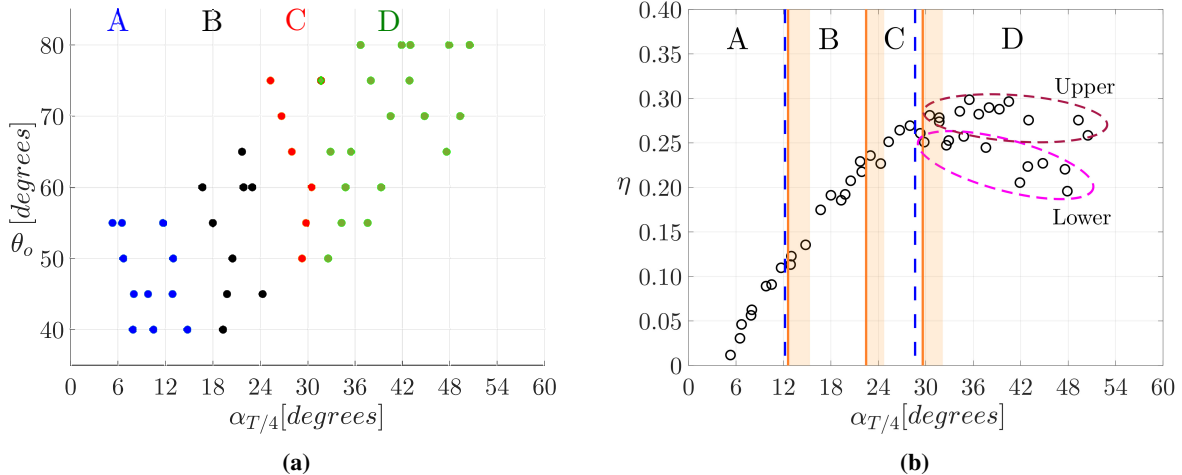


Fig. 11 (a) Clustering results represented by each foil kinematics as a data point: two kinematics with $\alpha_{T/4} = 31.7^\circ$ and $\theta_o = 75^\circ$ represented by a red circle and a green diamond placed in clusters C and D, respectively; (b) Updated class divisions (orange solid lines) compared with original groupings (blue dashed lines) along with the mismatch between class and cluster boundaries (orange shaded regions).

To summarize, when four classes are defined, the highest classification accuracy is obtained when the class boundaries are placed at $\alpha_{T/4} = 11.7^\circ$, $\alpha_{T/4} = 23.0^\circ$ and $\alpha_{T/4} = 29.3^\circ$ (orange lines from Figure 11b). The results of these tests reveal that the accuracy is just as good as the original three classes, with an average fold accuracy of 91%.

Furthermore, mismatched labels only occur close to the boundary divisions. For instance, 100% of the samples from class A in Folds 1 and 2 have a label match between predicted and prelabelled, with the same occurring in Fold 4 for classes B and C. For Fold 1, only the foil kinematics with $\alpha_{T/4} = 28.0^\circ$ is mislabelled between classes C and D, which can be explained by the proximity of this kinematics to its neighboring class. All other arrangements of class boundaries that are tested yield an average accuracy lower than 91%.

To illustrate the kinematics that are commonly mislabeled by the algorithm, the confusion matrix for the worst performance fold (fold 5) is displayed in Figure 12a. Even for this scenario, at least 79% of samples are properly labelled. Those not accurately predicted are shown in Figure 8b, with only a single foil kinematics with $\alpha_{T/4} = 31.7^\circ$ ($f^* = 0.15$; $h_o^* = 1.00$; $\theta_o = 75^\circ$) containing a label mismatch higher than 50%. An outlier is the kinematics with $\alpha_{T/4} = 5.3^\circ$ ($f^* = 0.15$; $h_o^* = 1.25$; $\theta_o = 55^\circ$) which contains a label mismatch lower than 50% and is not close to a neighbouring class. A possible explanation is the roll-up of the shear layer into multiple weak vortices generates a wake trajectory that is confused with the wake pattern of a higher $\alpha_{T/4}$. The wake structures found in this foil kinematics are displayed in Figure 5.

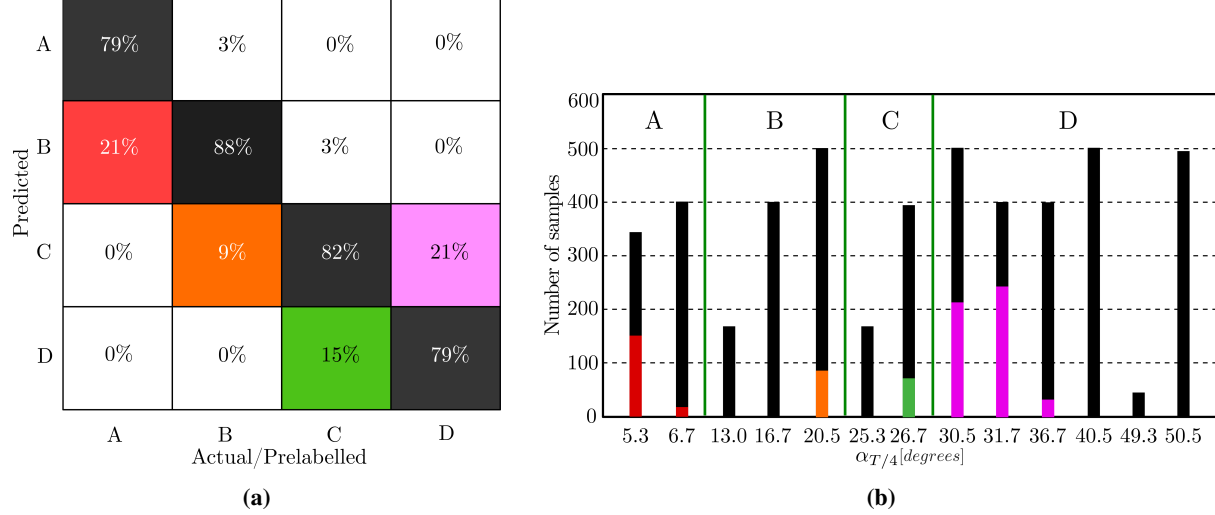


Fig. 12 (a) Confusion matrix for the worst performance (fold 5) with mislabeled class A samples colored in red; mislabeled class B in orange; mislabeled class C in green; mislabeled class D in pink. (b) Test set distribution of all foil kinematics in number of samples among $\alpha_{T/4}$ values presented in fold 5. The kinematics $f^* = 0.15$; $h_o^* = 1.00$; $\theta_o = 75^\circ$ is the only foil kinematics that had more than 50% of images with a label mismatch between actual and predicted. The green lines divide the data presented in each class.

The four updated classes offer new physical insight on wake patterns, illustrated in Figure 13. Each row highlights wake images at different foil positions that are randomly selected from various kinematics within each class. In class A ($5.3^\circ \leq \alpha_{T/4} \leq 11.7^\circ$), the foil generates a shear layer wake pattern as noticed by the absence of coherent vortices in the wake, and as previously described in Section III. Although classes B ($11.7^\circ < \alpha_{T/4} < 23.0^\circ$) and C ($23.0^\circ \leq \alpha_{T/4} \leq 29.3^\circ$) contain stronger vortices, the wake path is considerably different, with class B showing a longer wavelength within the selected wake window compared to class C (see yellow and red lines), which is a feature not previously captured by the original class divisions. Class D ($29.3^\circ < \alpha_{T/4} \leq 50.5^\circ$) contains kinematics where the foil generates the largest number and strongest coherent vortices, as shown by the presence of a strong primary LEV in the majority of wake images (see green circle). These differences in the wavelength among wake patterns emphasize the criteria used in unsupervised clustering to differentiate each regime which are not captured by the initial classification approach.

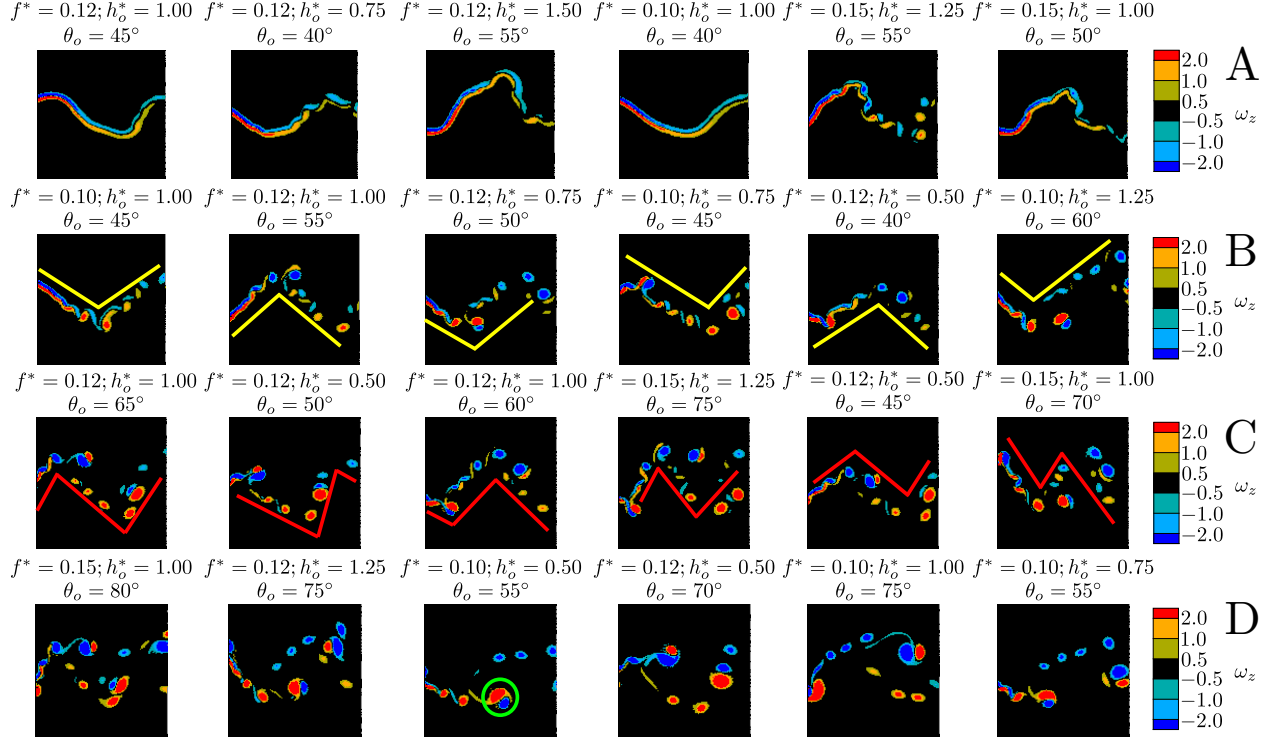


Fig. 13 Wake structures colored by spanwise vorticity (ω_z) for each class displayed in Figure 11b. The wake images are randomly selected within each class and the foil kinematics corresponding to each wake is displayed at top of each image. The yellow, red lines and green circle correspond to each wake pattern.

The wake patterns obtained by the classification and clustering models are significantly different from those found in propulsive foils. Comparing with previous work by Calvet et al. [25], they obtained six different wake patterns that are correlated with two parameters, $\alpha_{T/4}$ and Strouhal number ($St = \frac{2fh_o}{U_\infty}$), which varied from $0^\circ < \alpha_{T/4} < 40^\circ$ and $0.2 < St < 1.2$. Due to the higher reduced frequency of propulsive foils, more wake structures are found closer to the foil and this contributes to a higher contrast of wake patterns across clusters compared with those in Figure 13. This contrast also contributes to the difference in the number of wake patterns between foil regimes. While the work by Calvet et al. obtained six wake patterns behind propulsive foils, the analysis performed here identified four distinct wakes under the energy harvesting regime.

Class D demonstrates high variation in efficiency within its kinematics. This is observed between $\alpha_{T/4} = 40.5^\circ$ and $\alpha_{T/4} = 41.9^\circ$ where efficiency drops by approximately 9% (see Figure 11b). This could be described as a bifurcation in the efficiency curve at $\alpha_{T/4} > 28.0^\circ$ as illustrated by an upper and lower branches. However, neither the classification nor clustering models could discern differences in the wakes between the higher and lower branches of efficiency within class D. To further investigate these branches, the foil parameters corresponding to each kinematics are explored and it is noticed that all foil kinematics in the lower branch have a reduced frequency of $fc/U_\infty = 0.10$ and the upper branch, $fc/U_\infty = 0.12 - 0.15$.

The new updated classes also provide patterns in power extraction, as displayed in Figure 14. Each curve corresponds to the phase-averaged total power extracted in a half-cycle from a representative foil kinematics in each class. All classes display a power peak close to the mid-stroke position ($t/T = 0.25$), which corresponds to the foil's maximum heave velocity and thus typically is where maximum power is reached. Class A shows a smooth power profile with a lower amplitude compared to the other classes as expected due to the absence of coherent vortices generated by the foil. With the formation of LEVs as $\alpha_{T/4}$ increases, class B still highlights a smooth profile and class C indicates a higher power magnitude and higher unsteadiness on $t/T = 0.3 - 0.5$. This unsteady behavior is most likely caused by secondary vortices formed on the foil due to a higher $\alpha_{T/4}$ in class C compared to class B. This unsteadiness is more apparent in the lower branch of class D where large and strong vortices are formed and shed from the foil. The power profile in the representative kinematics of the upper branch is similar to the lower branch in the region $t/T = 0 - 0.3$ but it displays a second power peak in the remaining portion of the half-cycle. This peak is caused by the higher reduced frequency of the kinematics in the upper branch, which contributes to a delay in the vortex shedding and thus more power is extracted.

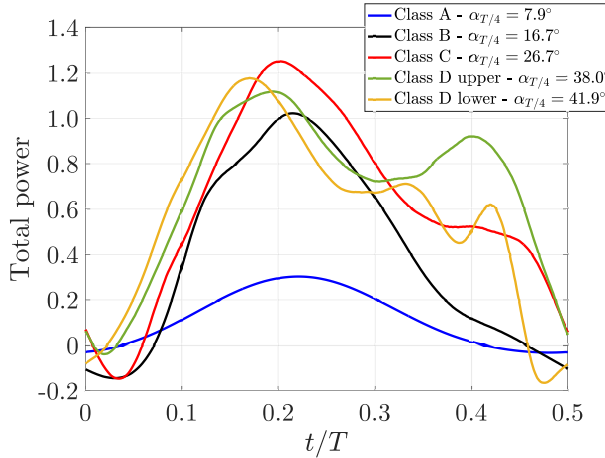


Fig. 14 Phase-averaged total power extracted in a half-cycle from a representative foil kinematics within each class.

To visualize those vortex structures, the wakes from both upper and lower branches are illustrated in Figure 15. As observed in Section III and by Ribeiro et al. [8], a lower reduced frequency is correlated with vortex structures spending less time on foil surface, which decreases the pressure gradient around the foil. The wake structures between upper and lower branches are different with more vortices located within the wake window in the upper branch due to higher foil's reduced frequency but still no pattern can be visualized. Although neither the classification nor clustering models could discern the differences just described in these branches, a possible solution would be to provide additional information about the kinematics of each wake image to the convolutional neural network like the reduced frequency, similar to the method implemented by Morimoto et al. [13], but it is not explored in this investigation. Another potential solution would be to have more foil kinematics and hence more data in class D.

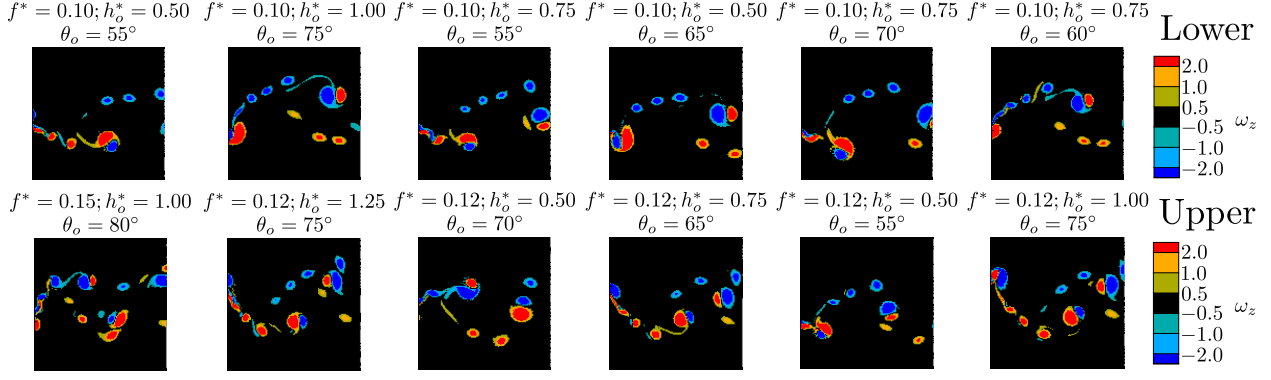


Fig. 15 Wake structures colored by spanwise vorticity (ω_z) that emerge from foil kinematics within each branch in class D highlighted in Figure 11b. The wake images are randomly selected and the foil kinematics corresponding to each wake is displayed at top of each image.

325 The wake patterns obtained from the updated classes can also be used to predict the power extraction of foil-arrays. For instance, the wake pattern generated from a class with low $\alpha_{T/4}$ values ($5.3^\circ \leq \alpha_{T/4} \leq 11.7^\circ$) does not significantly impact energy extraction from foils placed downstream due to the absence of coherent vortices that disturbs the oncoming flow of trailing foils. The opposite is true for a class with high $\alpha_{T/4}$ values ($29.3^\circ < \alpha_{T/4} \leq 50.5^\circ$).

VI. Conclusion

330 A machine learning model is developed to classify wake structures behind an oscillating foil in the energy harvesting regime of flapping foil kinematics. The goal of the paper is to utilize the machine learning algorithm to sort and classify wake modes using the vorticity fields downstream of the oscillating foil and correlate the kinematics with associated wake patterns. This model gives insight on wake similarity among various foil kinematics, which is important to build predictive models of oscillating foil arrays for energy harvesting.

335 Data is obtained through simulations of oscillating foils at 46 unique kinematics, and time-dependent vorticity flow fields are extracted at equal times across three simulation cycles to form a total of 23,692 samples. Based on previous work [9], three initial classes are defined based on values of the relative angle of attack, $\alpha_{T/4}$. The classification model consists of four convolutional layers and 90 LSTM units applied on multiple input sequences of five samples each. The model's output consists of three neurons corresponding to the classes A, B, C. After the model is trained and tuned, the 340 average test accuracy among all folds is 92% with the majority of foil kinematics showing a label mismatch percentage less than 50% between actual and predicted, demonstrating the model's ability to discern wakes among classes.

Although the classification model is successful in finding wake patterns the class divisions are predetermined by the researcher, and assumed to correlate with only one parameter, $\alpha_{T/4}$, thus biasing the relationship between wake structure and flapping kinematics. Therefore, an unsupervised approach is performed through a CAE clustering algorithm, which 345 does not require any prelabelling or bias. The results indicate that there is still a strong correlation with $\alpha_{T/4}$, and that

clusters naturally align with this kinematic parameter. Furthermore, analysis shows that four clusters are optimal instead of three that were originally proposed.

In summary, the clustering model provided validation that $\alpha_{T/4}$ was a predictive kinematic parameter for wake structure, and outlined an additional grouping previously undetected by the researcher. A final configuration of four new classes is proposed which results in an average fold accuracy of 91% using the classification algorithm. The four classes offer new physical insight on wake patterns within each range of foil kinematics based on vortex strength and oscillatory wake structure. Further analysis is performed in the class with the highest $\alpha_{T/4}$ values and additional wake patterns are obtained that could not be captured by either the classification or clustering algorithms. This research builds upon the knowledge of how wake patterns and kinematics are correlated, which is instrumental in developing predictive models of oscillating foil arrays in which vortex wakes directly impact the energy harvesting of downstream foils.

VII. Acknowledgments

This material is based upon work supported by the National Science Foundation under award CBET-1921594 and program director Ron Joslin. This research was conducted using computational resources and services at the Center for Computation and Visualization at Brown University. The authors thank Kenny Breuer for fruitful discussions on oscillating foil dynamics.

References

- [1] Young, J., Lai, J. C. S., and Platzer, M. F., "A review of progress and challenges in flapping foil power generation," *Progress in Aerospace Sciences*, Vol. 67, 2014. doi:10.1016/j.paerosci.2013.11.001.
- [2] Xiao, Q., and Zhu, Q., "A review on flow energy harvesters based on flapping foils," *Journal of Fluids and Structures*, Vol. 46, 2014. doi:10.1016/j.jfluidstructs.2014.01.002.
- [3] Oshkai, P., Iverson, D., Lee, W., and Dumas, G., "Reliability study of a fully-passive oscillating foil turbine operating in a periodically-perturbed inflow," *Journal of Fluids and Structures*, Vol. 113, 2022. doi:10.1016/j.jfluidstructs.2022.103630.
- [4] Williamson, C. H. K., and Roshko, A., "Vortex formation in the wake of an oscillating cylinder," *Journal of Fluids and Structures*, Vol. 2, 1988. doi:10.1016/S0889-9746(88)90058-8.
- [5] Schnipper, T., Andersen, A., and Bohr, T., "Vortex wakes of a flapping foil," *Journal of Fluid Mechanics*, Vol. 633, 2009. doi:10.1017/S0022112009007964.
- [6] Koochesfahani, M. M., "Vortical patterns in the wake of an oscillating airfoil," *AIAA Journal*, Vol. 27, 1989. doi:10.2514/3.10246.
- [7] Lai, J. C. S., and Platzer, M. F., "Jet Characteristics of a Plunging Airfoil," *AIAA Journal*, Vol. 37, 1999. doi:10.2514/2.641.
- [8] Ribeiro, B. L. R., Frank, S. L., and Franck, J. A., "Vortex dynamics and Reynolds number effects of an oscillating hydrofoil in energy harvesting mode," *Journal of Fluids and Structures*, Vol. 94, 2020. doi:10.1016/j.jfluidstructs.2020.102888.

[9] Ribeiro, B. L. R., Su, Y., Guillaumin, Q., Breuer, K. S., and Franck, J. A., “Wake-foil Interactions and Energy Harvesting Efficiency in Tandem Oscillating Foils,” *Physics Review Fluids*, Vol. 6, 2021. doi:10.1103/PhysRevFluids.6.074703.

[10] Brunton, S. L., Noack, B. R., and Koumoutsakos, P., “Machine Learning for Fluid Mechanics,” *Annual Review of Fluid Mechanics*, Vol. 52, 2020. doi:10.1146/annurev-fluid-010719-060214.

380 [11] Lee, S., and You, D., “Data-driven prediction of unsteady flow over a circular cylinder using deep learning,” *Journal of Fluid Mechanics*, Vol. 879, 2019. doi:10.1017/jfm.2019.700.

[12] Bhatnagar, S., Afshar, Y., Pan, S., Duraisamy, K., and Kaushik, S., “Prediction of aerodynamic flow fields using convolutional neural networks,” *Computational Mechanics*, Vol. 64, 2019. doi:10.1007/s00466-019-01740-0.

385 [13] Morimoto, M., Fukami, K., Zhang, K., Nair, A. G., and Fukagata, K., “Convolutional neural networks for fluid flow analysis: toward effective metamodeling and low-dimensionalization,” *arXiv preprint arXiv:2101.02535 [physics]*, 2021.

[14] Deng, L., Wang, Y., Liu, Y., Wang, F., Li, S., and Liu, J., “A CNN-based vortex identification method,” *Journal of Visualization*, Vol. 22, 2019. doi:10.1007/s12650-018-0523-1.

[15] Hunt, J., Wray, A., and Moin, P., “Eddies, streams, and convergence zones in turbulent flows,” *Center for Turbulence Research: Proceeding of the Summer Program*, 1988. URL <https://ntrs.nasa.gov/citations/19890015184>

390 [16] Jeong, J., and Hussain, F., “On the identification of a vortex,” *Journal of Fluid Mechanics*, Vol. 285, 1995. doi:10.1017/S0022112095000462.

[17] Hochreiter, S., and Schmidhuber, J., “Long Short-Term Memory,” *Neural Computation*, Vol. 9, 1997. doi:10.1162/neco.1997.9.8.1735.

395 [18] Han, R., Wang, Y., Zhang, Y., and Chen, G., “A novel spatial-temporal prediction method for unsteady wake flows based on hybrid deep neural network,” *Physics of Fluids*, Vol. 31, 2019. doi:10.1063/1.5127247.

[19] Nakamura, T., Fukami, K., Hasegawa, K., Nabae, Y., and Fukagata, K., “Convolutional neural network and long short-term memory based reduced order surrogate for minimal turbulent channel flow,” *Physics of Fluids*, Vol. 33, 2021. doi:10.1063/5.0039845.

400 [20] Zhang, J., and Zhao, X., “A novel dynamic wind farm wake model based on deep learning,” *Applied Energy*, Vol. 277, 2020. doi:10.1016/j.apenergy.2020.115552.

[21] Colvert, B., Alsalman, M., and Kanso, E., “Classifying vortex wakes using neural networks,” *Bioinspiration & Biomimetics*, Vol. 13, 2018. doi:10.1088/1748-3190/aaa787.

[22] Pollard, B., and Tallapragada, P., “Learning hydrodynamic signatures through proprioceptive sensing by bioinspired swimmers,” *Bioinspiration & Biomimetics*, Vol. 16, 2021. doi:10.1088/1748-3190/abd044.

405 [23] Li, B., Yang, Z., Zhang, X., He, G., Deng, B.-Q., and Shen, L., “Using machine learning to detect the turbulent region in flow past a circular cylinder,” *Journal of Fluid Mechanics*, Vol. 905, 2020. doi:10.1017/jfm.2020.725.

[24] Godoy-Diana, R., Aider, J.-L., and Wesfreid, J. E., “Transitions in the wake of a flapping foil,” *Physical Review E*, Vol. 77, 2008. doi:10.1103/PhysRevE.77.016308.

410 [25] Calvet, A. G., Dave, M., and Franck, J. A., “Unsupervised clustering and performance prediction of vortex wakes from bio-inspired propulsors,” *Bioinspiration & Biomimetics*, Vol. 16, 2021. doi:10.1088/1748-3190/ac011f.

[26] Kinsey, T., and Dumas, G., “Parametric Study of an Oscillating Airfoil in a Power-Extraction Regime,” *AIAA Journal*, Vol. 46, No. 6, 2008. doi:10.2514/1.26253.

[27] Kim, D., Strom, B., Mandre, S., and Breuer, K. S., “Energy harvesting performance and flow structure of an oscillating hydrofoil with finite span,” *Journal of Fluids and Structures*, Vol. 70, 2017. doi:10.1016/j.jfluidstructs.2017.02.004.

415 [28] Zhu, Q., “Optimal Frequency for Flow Energy Harvesting of a Flapping Foil,” *Journal of Fluid Mechanics*, Vol. 675, 2011, pp. 495–517. doi:10.1017/S0022112011000334.

[29] Weller, H. G., Tabor, G., Jasak, H., and Fureby, C., “A tensorial approach to computational continuum mechanics using object-oriented techniques,” *Computers in Physics*, Vol. 12, 1998. doi:10.1063/1.168744.

420 [30] Geuzaine, C., and Remacle, J.-F., “Gmsh: A 3-D finite element mesh generator with built-in pre- and post-processing facilities,” *International Journal for Numerical Methods in Engineering*, Vol. 79, 2009. doi:10.1002/nme.2579.

[31] Kinsey, T., and Dumas, G., “Optimal Tandem Configuration for Oscillating-Foils Hydrokinetic Turbine,” *Journal of Fluids Engineering*, Vol. 134, 2012. doi:10.1115/1.4005423.

[32] Ashraf, M. A., Young, J., Lai, J. C. S., and Platzer, M. F., “Numerical analysis of an oscillating-wing wind and hydropower generator,” *AIAA journal*, Vol. 49, 2011. doi:10.2514/1.J050577.

425 [33] Chong, Y. S., and Tay, Y. H., “Abnormal Event Detection in Videos Using Spatiotemporal Autoencoder,” *Advances in Neural Networks - ISNN 2017*, Vol. 10262, Springer International Publishing, 2017. doi:10.1007/978-3-319-59081-3_23.

[34] Abadi, M., Agarwal, A., Barham, P., Brevdo, E., Chen, Z., Citro, C., Corrado, G. S., Davis, A., Dean, J., Devin, M., Ghemawat, S., Goodfellow, I. J., Harp, A., Irving, G., Isard, M., Jia, Y., Józefowicz, R., Kaiser, L., Kudlur, M., Levenberg, J., Mané, D., Monga, R., Moore, S., Murray, D. G., Olah, C., Schuster, M., Shlens, J., Steiner, B., Sutskever, I., Talwar, K., Tucker, P. A., Vanhoucke, V., Vasudevan, V., Viégas, F. B., Vinyals, O., Warden, P., Wattenberg, M., Wicke, M., Yu, Y., and Zheng, X., “TensorFlow: Large-Scale Machine Learning on Heterogeneous Distributed Systems,” *CoRR*, 2016. ArXiv: abs/1603.04467.

430 [35] Chollet, F., et al., “Keras,” , 2015. URL <https://github.com/fchollet/keras>, Publisher: GitHub.

[36] Kingma, D. P., and Ba, J., “Adam: A Method for Stochastic Optimization,” *3rd International Conference on Learning Representations. ICLR 2015 - Conf. Track Proc*, 2015.

435 [37] Prechelt, L., “Automatic early stopping using cross validation: quantifying the criteria,” *Neural Networks*, Vol. 11, 1998.
doi:10.1016/S0893-6080(98)00010-0.

[38] Fukami, K., Fukagata, K., and Taira, K., “Assessment of supervised machine learning methods for fluid flows,” *Theoretical and Computational Fluid Dynamics*, Vol. 34, 2020. doi:10.1007/s00162-020-00518-y.

440 [39] Brunton, S. L., and Kutz, J. N., *Data-Driven Science and Engineering: Machine Learning, Dynamical Systems, and Control*, Cambridge University Press, 2019. doi:10.1017/9781108380690.

[40] Thorndike, R. L., “Who belongs in the family?” *Psychometrika*, Vol. 18, No. 4, 1953, pp. 267–276. doi:10.1007/BF02289263.

[41] Rousseeuw, P. J., “Silhouettes: A graphical aid to the interpretation and validation of cluster analysis,” *Journal of Computational and Applied Mathematics*, Vol. 20, 1987. doi:10.1016/0377-0427(87)90125-7.